Highly efficient sustainable photocatalytic Z-scheme hydrogen production from an α-Fe$_2$O$_3$ engineered ZnCdS heterostructure

M. Imran [a], Ammar Bin Yousaf [a,b,*], Peter Kasak [b], Akif Zeb [a], Syed Javaid Zaidi [b]

[a] Hefei National Laboratory for Physical Sciences at Microscale, University of Science and Technology of China, Hefei, Anhui 230026, People's Republic of China
[b] Center for Advanced Materials, Qatar University, Doha 2713, Qatar

ABSTRACT

We present an α-Fe$_2$O$_3$/Zn$_{0.4}$Cd$_{0.6}$S heterostructure that shows visible light photocatalytic H$_2$ production as high as 536.8 μmol h^{-1} with apparent quantum efficiency of 11.2% at 420 nm. The UV–vis diffuse reflectance spectra of as-synthesized α-Fe$_2$O$_3$/Zn$_{0.4}$Cd$_{0.6}$S heterostructure reveal efficient absorption in the visible region, which is a key factor in the enhanced catalytic activity. Moreover, the increase in charge separation efficiency of α-Fe$_2$O$_3$/Zn$_{0.4}$Cd$_{0.6}$S suggested by electrochemical impedance spectroscopy and photocurrent response also results in enhanced photocatalytic H$_2$ production. The interface contact between α-Fe$_2$O$_3$ and Zn$_{0.4}$Cd$_{0.6}$S ascertained from HRTEM images promotes the recombination of photogenerated electrons from the conduction band of α-Fe$_2$O$_3$ and holes from the valence band of Zn$_{0.4}$Cd$_{0.6}$S, thus enhancing the utilization of solar light and increasing the efficiency. Our coupling approach to synthesizing an efficient Z-scheme photocatalyst provides insight into the design of further solar energy utilization photocatalysts.

© 2017 Elsevier Inc. All rights reserved.

1. Introduction

Over the past century, growing global energy demands have forced researchers to find renewable energy resources to substitute for limited fossil fuel [1]. Among various methods reported so far, artificial photosynthetic systems for hydrogen production from photocatalytic water splitting are promising candidates for clean energy generation [2]. Numerous attempts to design and synthesize efficient photocatalysts with suitable band gaps and high efficiency for hydrogen production have been reported [3]. However, most photocatalysts, due to their wide band gaps, can only utilize ultraviolet irradiation for hydrogen production, which constitutes a small fraction of the incoming solar light [4,5]. To maximize the benefit of incoming solar light, photocatalysts that can absorb visible light must be developed.

The key features of efficient visible-light-driven photocatalysts are wide absorption range in the visible region, high charge separation efficiency, strong redox ability, and long-term stability, which is difficult for a single-component photocatalyst to possess [6]. To synthesize such a photocatalyst, a multicomponent Z-scheme photocatalytic system was introduced by Bard et al. in 1979 [7]. This system was inspired by natural photosynthesis in green plants by introducing two different photocatalysts in one system that features the spatial isolation of photogenerated electrons and holes and reduces electron–hole recombination. Z-scheme photocatalytic system with better hydrogen production efficiency using various combinations of photocatalysts have been reported recently [8]. However, some still needed expensive noble metals as mediators while others had poor recyclability, which makes the systems useless in practical applications [9,10].

Solid-solution-based photocatalysts such as zinc sulfide (ZnS), cadmium sulfide (CdS), and ZnS–CdS, have attracted much attention of researchers due to their excellent properties for visible light absorption [11,12]. CdS showed good performance in photocatalytic hydrogen generation, as its band gap corresponds well to the solar spectrum. However, the undesired photocorrosion properties of CdS limit its practical use, and therefore it is essential to build a hybrid photocatalyst by combining CdS with some other materials [13]. On the other hand, ZnS, with a band gap of 3.6 eV, provides an excellent opportunity to make a hybrid photocatalyst, as its band level is high enough to reduce water into H$_2$ [14]. The high negative potential of excited electrons in ZnS also allows hydrogen production without the assistance of noble metals as co-catalysts. Some groups have successfully synthesized Zn$_{1-x}$Cd$_x$S photocatalysts with good photocatalytic properties for water splitting [15]. However, there are few reports regarding the

* Corresponding author at: Hefei National Laboratory for Physical Sciences at Microscale, University of Science and Technology of China, Hefei, Anhui 230026, People's Republic of China.

E-mail addresses: ammar@mail.ustc.edu.cn, muhammad.ammar@qu.edu.qa, ammar.chemist18@gmail.com (A.B. Yousaf).

room-temperature synthesis of $Zn_{1-x}Cd_xS$ with excellent photocatalytic efficiencies. Moreover, to synthesize an excellent photocatalyst with optimum band gap, a heterostructure has to be considered, as the heterostructure is expected to promote charge transfer through interface contact with better charge separation efficiency [16,17].

Hematite (α-Fe_2O_3) is also considered an excellent photocatalyst because of its narrow band gap (2.1 eV) for hydrogen production through solar water splitting. Hematite absorbs a large fraction (ca. 13.5%) of solar light and is of low cost, nontoxic, environmentally friendly, and highly stable in alkaline solutions [18]. However, the practical use of α-Fe_2O_3 for photocatalytic hydrogen production is limited due to its low electron mobility (10^{-2} to 10^{-1} cm^2 V^{-1} s^{-1}), short hole diffusion length (2–4 nm), and short lifetime of charge carriers (about 10 ps) [19]. Different methods have been reported for improving its photocatalytic properties, such as introduction of a co-catalyst and doping with noble metals; however, none of them proved to be useful in practical applications [20–22]. An effective way to address these problems may be provided by coupling α-Fe_2O_3 and $Zn_{0.4}Cd_{0.6}S$ to construct an interface connection for direct Z-scheme electron transportation, as presented by Mirtchev et al. [23].

In this study, we present an advance in photocatalytic hydrogen generation from our synthesized α-Fe_2O_3/$Zn_{0.4}Cd_{0.6}S$ heterostructure. We followed a simple approach for the synthesis. Two photocatalysts (α-Fe_2O_3, $Zn_{0.4}Cd_{0.6}S$) are coupled to synthesize a multicomponent Z-scheme photocatalytic system with an interface connection.

2. Experimental

2.1. Chemicals

Polyvinylpyrrolidone (M.W. 8000) and $FeCl_3$·$6H_2O$ were purchased from Alfa Aesar. Sodium acetate (CH_3COONa), zinc acetate ($Zn(CH_3COO)_2$·$2H_2O$), cadmium acetate ($Cd(CH_3COO)_2$·$2H_2O$), sodium sulfide nonahydrate (Na_2S·$9H_2O$), and sodium sulfite (Na_2SO_3) were purchased from Sinopharm Chemical Reagent. All other chemical reagents were of analytical grade and used as received without further purification.

2.2. Characterization

The morphology of the particles was observed by scanning electron microscopy (SEM, JSM 6700F, JEOL). Transmission electron microscopic (TEM) images and high-resolution transmission electron microscopic (HRTEM) images were obtained on a JEM-2100F field emission electron microscope at an accelerating voltage of 200 kV. The high-angle annular dark-field scanning transmission electron microscopy (HAADF-STEM) image and energy-dispersive X-ray (EDX) mapping images were obtained on a JEOL JEM-ARF200F atomic resolution analytical microscope. The X-ray powder diffraction (XRD) patterns of the products were determined on a Philips X'Pert Pro Super diffractometer with CuKα radiation (λ = 1.54178 Å). The operating voltage was maintained at 40 kV and the current at 200 mA, respectively. X-ray photoelectron spectroscopy (XPS) was carried out on a Perkin Elmer RBD upgraded PHI-5000C ESCA system. A Shimadzu spectrophotometer (Model 2501 PC) was used to record the UV−vis diffuse reflectance spectra of the samples in the region 200–800 nm. Nitrogen adsorption measurements were obtained at 77 K with a Micromeritics ASAP 2020 system using Barrett–Emmett–Teller (BET) calculations for the surface area. The elemental analysis was also carried out on an inductively coupled plasma mass spectrometer (ICP-MS, Perki-nElmer, ELAN 6000). The Fourier transform infrared (FT-IR) spectra

(KBr disk, 4000–400 cm^{-1}) were recorded on a Bruker EQUINOX55 FT-IR spectrophotometer. Thermogravimetric analyses were performed under N_2 at a heating rate of 10 °C min^{-1} with a Shimadzu TGA-50H thermogravimetric analyzer.

2.3. Synthesis of α-Fe_2O_3 nanoparticles

A hydrothermal route was followed to synthesize α-Fe_2O_3 nanoparticles. In a typical synthesis, 1.0 g of polyvinylpyrrolidone (MW 8000) was dissolved in 30 mL of distilled water; then 2 mmol of $FeCl_3$·$6H_2O$ and 50 mmol of sodium acetate were added and the mixture was stirred for 2 h at room temperature. After that, the mixture was transferred to a stainless steel Teflon-lined autoclave and heated at 210 °C for 20 h. After the autoclave was cooled to room temperature, a red product was obtained, which was washed with distilled water and ethanol and dried in a vacuum oven at 60 °C overnight.

2.4. Synthesis of α-Fe_2O_3/$Zn_{0.4}Cd_{0.6}S$ heterostructures

In a typical synthesis, 4 mmol of zinc acetate, 6 mmol of cadmium acetate, and a certain amount of α-Fe_2O_3 (5, 10, or 15 wt. %) were added to 150 ml of distilled water. The pH of the solution was adjusted to 7.4 using a 0.1 M sodium hydroxide solution. After 15 min, 12 mmol of sodium sulfide nonahydrate dissolved in 90 mL of distilled water was added dropwise into the above solution with continuous stirring. The resultant mixture was stirred at room temperature for 24 h. The obtained powders were washed with water and ethanol at least three times and dried in a vacuum oven at 60 °C overnight. Finally, the obtained powders were calcined for 2 h at different temperatures (573, 673, or 773 K) under a nitrogen flow with a heating rate of 5 °C/min. Bare $Zn_{0.4}Cd_{0.6}S$ nanoparticles were prepared following the same procedure except for the use of α-Fe_2O_3. The characterizations of α-Fe_2O_3/$Zn_{0.4}Cd_{0.6}S$ heterostructures were performed after heat treatment at 673 K for 2 h under nitrogen flow.

2.5. Photocatalytic reaction

The photocatalytic hydrogen (H_2) production reactions from water were carried out in a high-vacuum, gas-closed circulation system using a 300 W Xe lamp equipped with a cutoff filter ($\lambda \geq 420$ nm) to remove UV light. The average light intensity was 2.84 mW/cm^2. In a typical experiment, 100 mg of catalyst was dispersed in an aqueous solution (100 ml) containing 0.1 M Na_2S and 0.1 M Na_2SO_3. Online gas chromatography (Agilent 6820, TCD detector, N_2 carrier) was used to determine the amount of hydrogen evolved and compared with results from other samples.

2.6. Quantum efficiency measurement

Apparent quantum yields (AQYs) were determined using a 420 nm bandpass filter. The number of incident photons from the Xenon lamp was measured with a power meter (1831-R, Newport). AQYs were calculated by the following equation:

$$AQY\ (\%) = \frac{2 \times \text{The number of evolved } H_2 \text{ molecules}}{\text{The number of incident photons}} \times 100.$$

2.7. Electrochemical and photoelectrochemical measurements

Electrochemical and photoelectrochemical measurements were conducted in a 0.1 M Na_2SO_4 electrolyte solution in a three-electrode quartz cell. Ag/AgCl was used as a reference electrode, while a platinum wire was used as counter electrode and catalyst

film electrodes on Ti foil served as working electrodes. The catalyst films were prepared by dropping catalyst suspensions (10 mg mL^{-1} in ethanol) onto Ti foil following the doctor-blade coating method with a glass rod and Scotch tape, and the resultant electrodes were annealed for 12 h at 90 °C. For the measurements, the electrodes were pressed against a square shaped electrochemical cell with a working area of 4.0 cm^2. Photoelectrochemical test systems were composed of a CHI 660B electrochemistry potentiostat (Shanghai Chenhua Limited, China).

3. Results and discussion

The size and morphology of as-synthesized α-Fe$_2$O$_3$, Zn$_{0.4}$Cd$_{0.6}$S, and α-Fe$_2$O$_3$/Zn$_{0.4}$Cd$_{0.6}$S heterostructure were observed by SEM and TEM (Fig. 1, Fig. S1). Fig. S1 shows SEM images of α-Fe$_2$O$_3$ and Zn$_{0.4}$Cd$_{0.6}$S; the α-Fe$_2$O$_3$ nanoparticles are nanospheres with a size of about 20 nm, while Zn$_{0.4}$Cd$_{0.6}$S are irregular-shaped nanoparticles having average size 10 nm. Fig. 1a shows a SEM image of a 10 wt.% α-Fe$_2$O$_3$/Zn$_{0.4}$Cd$_{0.6}$S heterostructure; the α-Fe$_2$O$_3$ is well surrounded by Zn$_{0.4}$Cd$_{0.6}$S nanoparticles. The hybrid heterostructure comprises an interconnected well-defined network of α-Fe$_2$O$_3$ and Zn$_{0.4}$Cd$_{0.6}$S nanoparticles with uniform distribution of α-Fe$_2$O$_3$ throughout the Zn$_{0.4}$Cd$_{0.6}$S nanostructure. A tapping-mode atomic force microscopy (AFM) image of the as-synthesized 10 wt.% α-Fe$_2$O$_3$/Zn$_{0.4}$Cd$_{0.6}$S heterostructure along, with its size distribution and grain size, are shown in Figs. S2 and S3. The particles are of varying size and uniformly distributed. Intimate interfacial contact between α-Fe$_2$O$_3$ and Zn$_{0.4}$Cd$_{0.6}$S is observed in the form of defined grain boundaries. A low-magnification TEM image of the 10 wt.% α-Fe$_2$O$_3$/Zn$_{0.4}$Cd$_{0.6}$S heterostructure is shown in Fig. 1b. The α-Fe$_2$O$_3$ nanoparticles are randomly surrounded by Zn$_{0.4}$Cd$_{0.6}$S nanoparticles, forming a compact structure. The intimate contact of the α-Fe$_2$O$_3$ nanoparticles with Zn$_{0.4}$Cd$_{0.6}$S nanoparticles was assessed by HRTEM, which indicates the homogeneous distribution of α-Fe$_2$O$_3$ nanoparticles over Zn$_{0.4}$Cd$_{0.6}$S, composing a hybrid material (Fig. 1c). A STEM image of the α-Fe$_2$O$_3$/Zn$_{0.4}$Cd$_{0.6}$S heterostructure shows that α-Fe$_2$O$_3$ nanoparticles are surrounded by Zn$_{0.4}$Cd$_{0.6}$S (Fig. 1d). These results clearly demonstrate that α-Fe$_2$O$_3$/Zn$_{0.4}$Cd$_{0.6}$S heterostructures with strong interface coupling were successfully fabricated, which is favorable for improving the charge carrier separation between the photocatalysts and thus the photocatalytic activity. In addition, HAADF-STEM element mappings were further performed and it can be seen clearly from Fig. 2 that Zn, Cd, S, Fe, and O are evenly distributed, indicating the formation of hybrid nanostructure. The EDX spectrum was also used to confirm the existence of Zn, Cd, S, Fe, and O; the atomic ratio of Zn:Cd was observed to be 0.4:0.6, which is in agreement with the experimental data and XPS results (Fig. S4).

The XRD patterns of as-synthesized samples are presented in Fig. 3. The results show that the diffraction peaks of α-Fe$_2$O$_3$ can be readily indexed to rhombohedral hematite (α-Fe$_2$O$_3$; JCPDS 33-0664) with space group of R-3c having lattice parameters a = 5.0357 Å and c = 13.7488 Å [24]. Three prominent diffraction peaks appeared in the XRD pattern of Zn$_{0.4}$Cd$_{0.6}$S and 10 wt.% α-Fe$_2$O$_3$/Zn$_{0.4}$Cd$_{0.6}$S measured in the scan range 10–70. The peaks at 28.1°, 45.7°, and 53.9° matched well the (1 1 1), (2 2 0), and (3 1 1) planes of the zinc blend phase, respectively [25]. The diffraction peaks of α-Fe$_2$O$_3$ in the α-Fe$_2$O$_3$/Zn$_{0.4}$Cd$_{0.6}$S heterostructure were not more prominent, likely due to the low α-Fe$_2$O$_3$ content in the nanostructure.

XPS analysis of Zn$_{0.4}$Cd$_{0.6}$S and 10 wt.% α-Fe$_2$O$_3$/Zn$_{0.4}$Cd$_{0.6}$S was performed to reveal the presence of elements. Results are shown in Figs. S5 and 4, respectively. Survey XPS spectra of Zn$_{0.4}$Cd$_{0.6}$S shown in Fig. S5a indicate the presence of Zn, Cd, and S in the Zn$_{0.4}$Cd$_{0.6}$S sample. High-resolution spectra of Zn2p, Cd3d, and S2p are also displayed in Figs. S5b, S5c, and S5d, respectively. The Zn2p spectrum depicts peaks at binding energies of 1023.6 and 1046.8 eV for Zn2p$_{3/2}$ and Zn2$p_{1/2}$, respectively. The binding energies corresponding to Cd3d5/2 and 3d3/2 are found to be 405.1 and
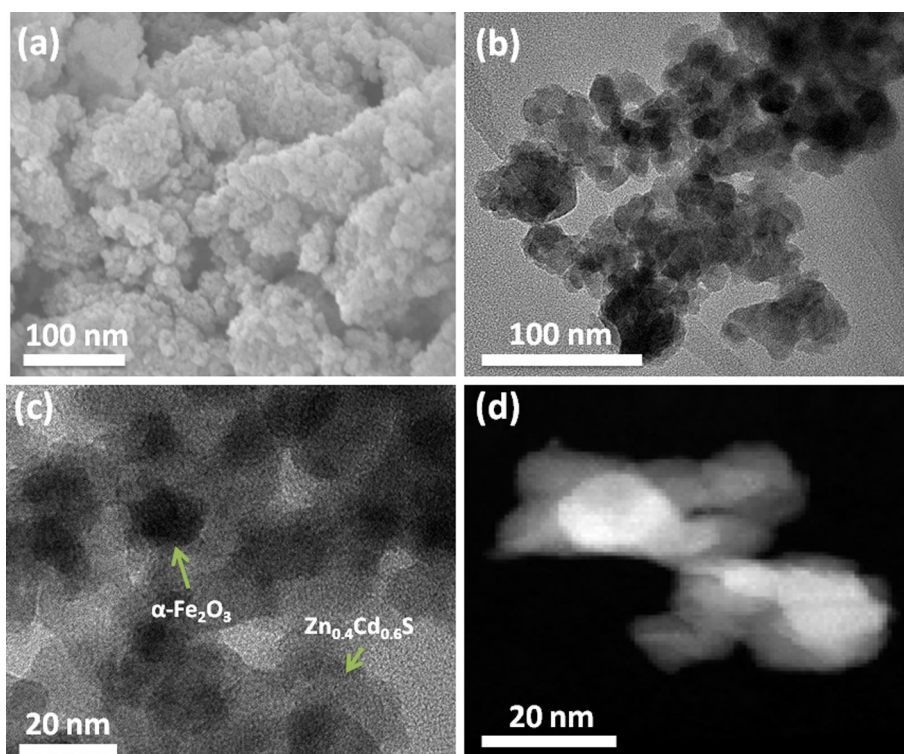

Fig. 1. SEM image (a), TEM image (b), HRTEM image (c), and STEM image of the 10 wt.% α-Fe$_2$O$_3$/Zn$_{0.4}$Cd$_{0.6}$S heterostructure.
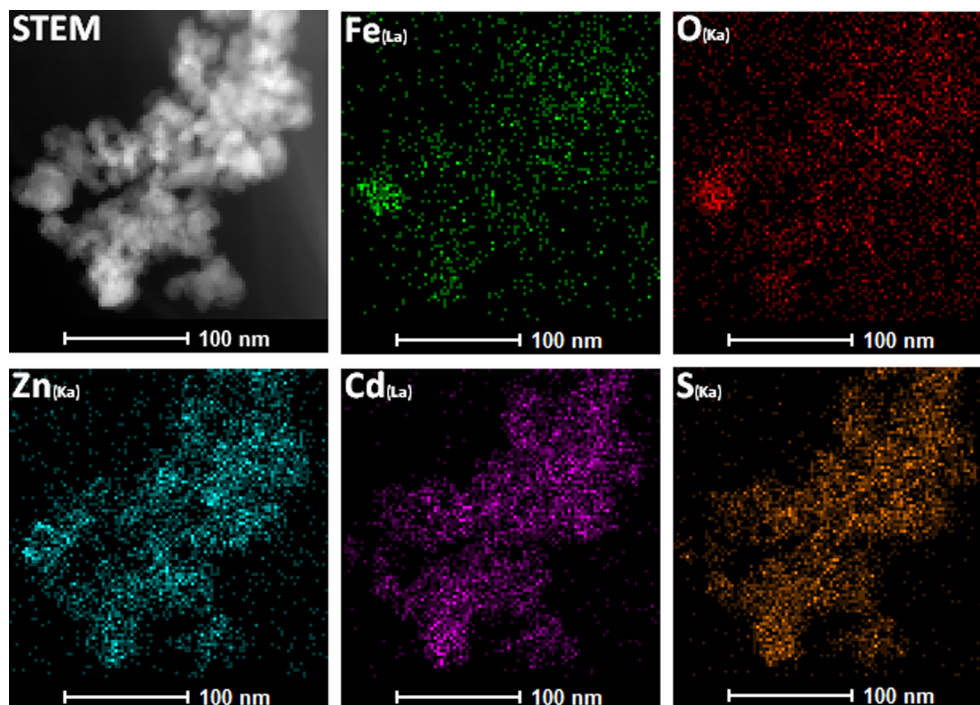
Fig. 2. HAADF-STEM element mapping images of the 10 wt.% α-Fe$_2$O$_3$/Zn$_{0.4}$Cd$_{0.6}$S heterostructure with Fe$_{(La)}$, O$_{(Ka)}$, Zn$_{(Ka)}$, Cd$_{(La)}$, and S$_{(Ka)}$ shown in different colors.
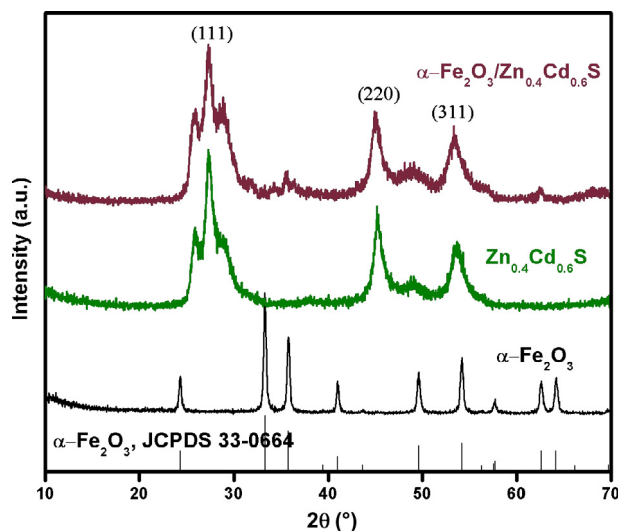
Fig. 3. XRD patterns of as-synthesized α-Fe$_2$O$_3$, Zn$_{0.4}$Cd$_{0.6}$S, and 10 wt.% α-Fe$_2$O$_3$/Zn$_{0.4}$Cd$_{0.6}$S heterostructure.

411.8 eV, respectively which is in agreement with the literature [26]. The high-resolution XPS spectrum of S2p is shown in Fig. S2d, which exhibits a broad peak at 161.3 eV corresponding to S^{2-} [27]. The Zn:Cd ratio obtained from XPS analysis is well matched with the experimental calculations and EDX results. A typical survey XPS spectrum of 10 wt.% α-Fe$_2$O$_3$/Zn$_{0.4}$Cd$_{0.6}$S is also shown in Fig. 4a, which indicates the presence of Zn, Cd, S, Fe, and O. As shown in Fig. 4b, the binding energies of the Zn2p3/2 and 2p1/2 peaks at 1023.8 and 1046.9 eV, respectively, matched reported data well [26]. Fig. 4c shows the Cd3d spectral binding energy region, in which peaks at 405.2 and 411.9 eV are in agreement with Cd3d5/2 and 3d3/2, respectively. The S^{2-} peak at binding energy 161.4 eV also indicates the presence of S in the 10 wt.% α-Fe$_2$O$_3$/Zn$_{0.4}$Cd$_{0.6}$S sample (Fig. 4d). The typical high-resolution

O1s spectra shown in Fig. 4e can be further deconvoluted into three Gaussian curves centered at 530.1, 531.5, and 532.8 eV. The low-binding-energy component is ascribed to the O^{2-} ions in α-Fe$_2$O$_3$, while the component in the higher-binding-energy region is related to the O—C and physisorbed water molecules. High-resolution Fe spectra of the 10 wt.% α-Fe$_2$O$_3$/Zn$_{0.4}$Cd$_{0.6}$S sample are also shown in Fig. 4f, which indicates peaks at 712.0 and 724.4 eV, confirming the presence of Fe2$p_{3/2}$ and 2$p_{1/2}$, respectively [28]. The shakeup satellite at 719.9 eV was the typical Fe^{3+} in α-Fe$_2$O$_3$/Zn$_{0.4}$Cd$_{0.6}$S. The very-low-intensity peaks of Fe2p and oxygen bound to Fe are a clear indication of the low loading amount of α-Fe$_2$O$_3$ and of most of α-Fe$_2$O$_3$ being surrounded by Zn$_{0.4}$Cd$_{0.6}$S nanoparticles. A typical survey XPS spectrum of α-Fe$_2$O$_3$ nanoparticles is also shown in Fig. S6a, which shows the presence of Fe and O orbitals. High-resolution Fe spectra of α-Fe$_2$O$_3$ nanoparticles indicate the existence of Fe2$p_{3/2}$ and 2$p_{1/2}$ peaks centered at 711.8 and 724.6 eV, respectively; the binding energies are in agreement with the 10 wt.% α-Fe$_2$O$_3$/Zn$_{0.4}$Cd$_{0.6}$S sample (Fig. S6b). The high-resolution O1s spectra shown in Fig. S6c can be further deconvoluted into three Gaussian curves centered at 529.8, 531.2, and 532.3 eV. The low-binding-energy component is ascribed to the O^{2-} ions in α-Fe$_2$O$_3$, while the component in the higher-binding-energy region is related to the physisorbed water molecules and carbon components.

The UV–vis diffuse reflectance spectra of α-Fe$_2$O$_3$, Zn$_{0.4}$Cd$_{0.6}$S, and 10 wt.% α-Fe$_2$O$_3$/Zn$_{0.4}$Cd$_{0.6}$S were also recorded to find the visible absorption capacity and are given in Fig. 5. The pure α-Fe$_2$O$_3$ nanoparticles show strong absorption in the visible light region, having a band gap of 2.1 eV, while the as-obtained Zn$_{0.4}$Cd$_{0.6}$S nanoparticles can absorb visible light with wavelengths of about 475 nm, which corresponds to a band gap of 2.61 eV. The 10 wt.% α-Fe$_2$O$_3$/Zn$_{0.4}$Cd$_{0.6}$S heterostructure shows a deep orange color and wide intense absorption in the visible region, which is beneficial for the photocatalytic performance of the heterostructure. The calculated band gap for the 10 wt.% α-Fe$_2$O$_3$/Zn$_{0.4}$Cd$_{0.6}$S heterostructure is 1.8 eV, which is above the minimum band gap limit suitable for water splitting. The photocurrent response curves
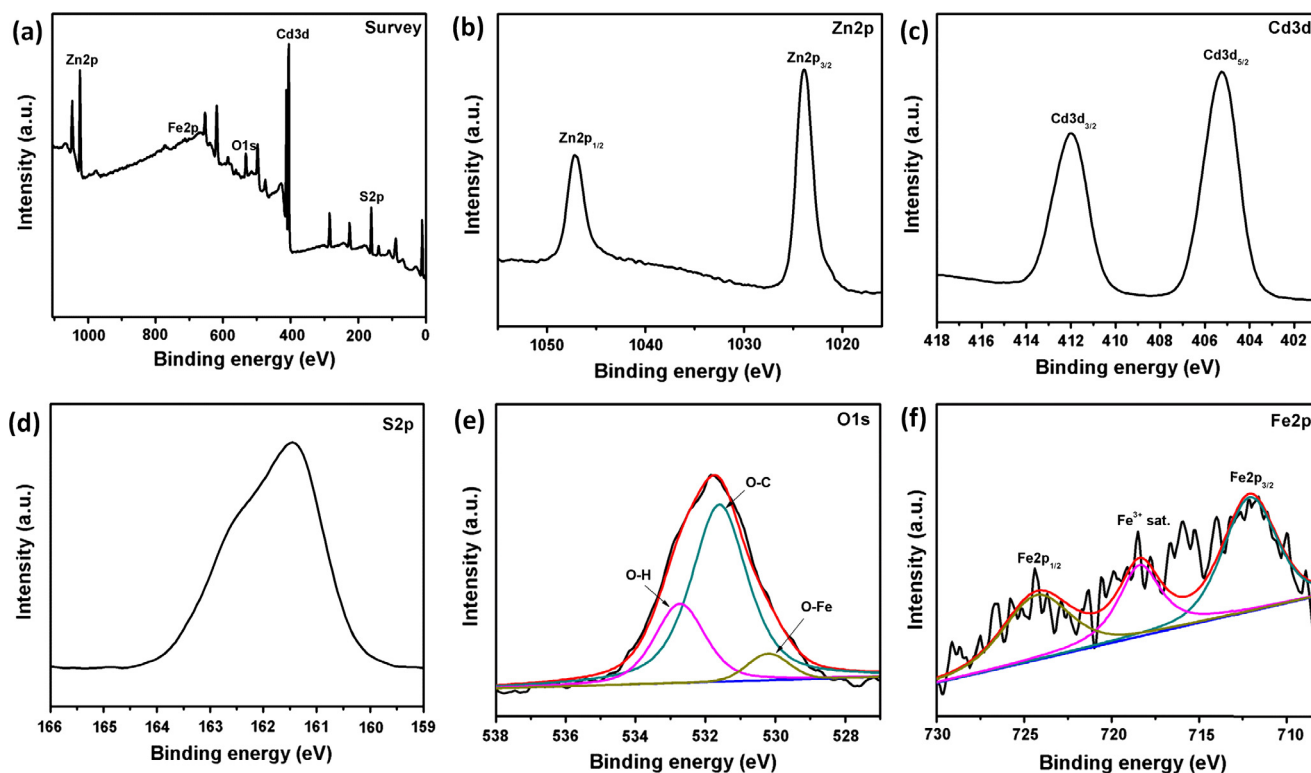
Fig. 4. XPS spectra of 10 wt.% α-Fe$_2$O$_3$/Zn$_{0.4}$Cd$_{0.6}$S heterostructure: survey spectrum (a), Zn2p orbitals (b), Cd3d orbitals (c), S2p orbitals (d), O1s orbitals (e), and Fe2p orbitals (f).
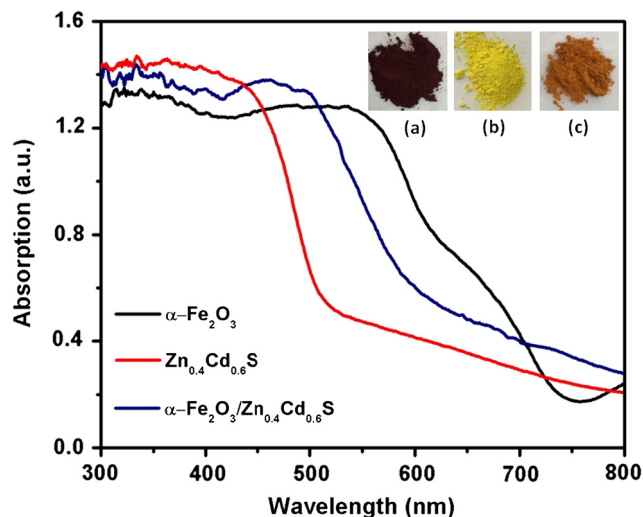

Fig. 5. UV–visible diffuse reflectance spectra of α-Fe$_2$O$_3$, Zn$_{0.4}$Cd$_{0.6}$S, and 10 wt.% α-Fe$_2$O$_3$/Zn$_{0.4}$Cd$_{0.6}$S; the inset is the photographs of α-Fe$_2$O$_3$ (a), Zn$_{0.4}$Cd$_{0.6}$S (b), and 10 wt.% α-Fe$_2$O$_3$/Zn$_{0.4}$Cd$_{0.6}$S (c).

of α-Fe$_2$O$_3$, Zn$_{0.4}$Cd$_{0.6}$S, and 10 wt.%) α-Fe$_2$O$_3$/Zn$_{0.4}$Cd$_{0.6}$S were also analyzed using A photoelectrochemical test device by dropping the sample dispersions onto Ti foil (see the Section 2). The current value increases to a maximum when the light is turned on, which is due to the separation of electron–hole pairs at the semiconductor–electrolyte interface, while the current value decreases to zero when the light turned is off, which may be ascribed to the recombination of electron–hole pairs. It can be clearly seen from Fig. 6a that the α-Fe$_2$O$_3$/Zn$_{0.4}$Cd$_{0.6}$S heterostructure exhibits a high photocurrent response as compared with α-Fe$_2$O$_3$ and Zn$_{0.4}$Cd$_{0.6}$S. The high photocurrent response in 10 wt.% α-Fe$_2$O$_3$/Zn$_{0.4}$Cd$_{0.6}$S

photocatalyst is attributed to low electron–hole pair recombination as electrons shift from the conduction band of α-Fe$_2$O$_3$ to the valence band of Zn$_{0.4}$Cd$_{0.6}$S, resulting in higher photocatalytic performance [29]. To further gain insight into the interface charge separation efficiency of the as-synthesized α-Fe$_2$O$_3$/Zn$_{0.4}$Cd$_{0.6}$S heterostructure, we performed electrochemical impedance spectroscopy (EIS). The Nyquist plots for α-Fe$_2$O$_3$, Zn$_{0.4}$Cd$_{0.6}$S, and 10 wt.% α-Fe$_2$O$_3$/Zn$_{0.4}$Cd$_{0.6}$S are shown in Fig. 6b. The Nyquist plots of α-Fe$_2$O$_3$/Zn$_{0.4}$Cd$_{0.6}$S showed a much smaller semicircle with the lowest Rct compared with the α-Fe$_2$O$_3$, Zn$_{0.4}$Cd$_{0.6}$S, which suggests an increase in charge separation efficiency, resulting in enhanced photocatalytic H$_2$ production [30,31]. The EIS results are in consistent with the photocurrent response data, which suggest that the high photocatalytic activity of α-Fe$_2$O$_3$/Zn$_{0.4}$Cd$_{0.6}$S originates from efficient charge separation and mobility of photoinduced charge carriers [32]. To be useful in practical applications, a photocatalyst should have high charge-separation efficiency, strong absorption in the visible range, and long-term stability for multiple cycles to work effectively; a single-component photocatalyst may not have all these features. Herein, our strategy to develop a multicomponent Z-scheme photocatalyst proves to be working, as the key features of an efficient photocatalyst are exhibited by our photocatalyst. The α-Fe$_2$O$_3$/Zn$_{0.4}$Cd$_{0.6}$S heterostructure shows strong absorption in the visible region and high charge efficiency, as indicated from photocurrent response and EIS results. The interface contact between α-Fe$_2$O$_3$ and Zn$_{0.4}$Cd$_{0.6}$S promotes the recombination of photogenerated electrons from the conduction band of Photosystem II (α-Fe$_2$O$_3$) and holes from the valence band of Photosystem I (Zn$_{0.4}$Cd$_{0.6}$S) and balances the distribution of incident photons between the two photosystems, thus enhancing the utilization of solar light and increasing the efficiency.

The visible light photocatalytic H$_2$ evolution rate over different loading amounts of α-Fe$_2$O$_3$ in the α-Fe$_2$O$_3$/Zn$_{0.4}$Cd$_{0.6}$S heterostruc-
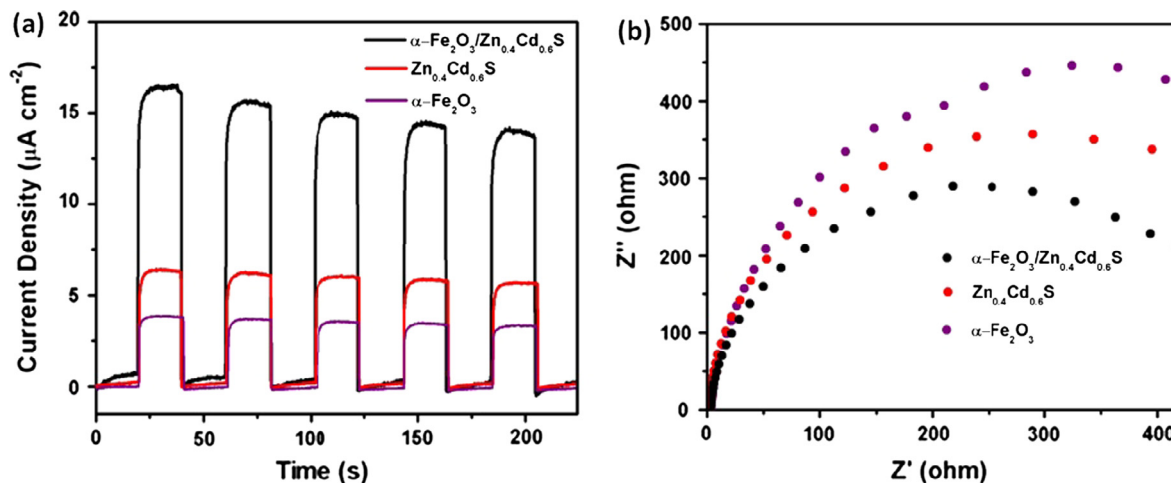
Fig. 6. Photocurrent response vs. time for α-Fe$_2$O$_3$, Zn$_{0.4}$Cd$_{0.6}$S, and 10 wt.% α-Fe$_2$O$_3$/Zn$_{0.4}$Cd$_{0.6}$S samples ($\lambda \geq 420$ nm) (a); EIS curves of α-Fe$_2$O$_3$, Zn$_{0.4}$Cd$_{0.6}$S, and 10 wt.% α-Fe$_2$O$_3$/Zn$_{0.4}$Cd$_{0.6}$S.

ture were measured in the presence of Na$_2$S and Na$_2$SO$_3$ as sacrificial reagents and are provided in Fig. 7a. Zn$_{0.4}$Cd$_{0.6}$S alone exhibits moderate photocatalytic activity with an H$_2$ evolution rate of 22.4 µmol h^{-1}, while the introduction of α-Fe$_2$O$_3$ leads to an enhancement in the H$_2$ evolution rate. The loading amount of α-Fe$_2$O$_3$ in the heterostructure plays an important role in the photocatalytic activity: As the amount of α-Fe$_2$O$_3$ increases from 5 to 10 wt.%, the H$_2$ evolution rate of α-Fe$_2$O$_3$/Zn$_{0.4}$Cd$_{0.6}$S is enhanced from 265.5 to 536.8 µmol h^{-1} with AQY of 11.2% at 420 nm, suggesting efficient charge separation and enhancement in the recombination of photogenerated electrons from the conduction band of α-Fe$_2$O$_3$ and holes from the valence band of Zn$_{0.4}$Cd$_{0.6}$S [33]. Further increasing the α-Fe$_2$O$_3$ amount in α-Fe$_2$O$_3$/Zn$_{0.4}$Cd$_{0.6}$S leads to a decrease in photocatalytic activity, as Zn$_{0.4}$Cd$_{0.6}$S is a major component of the Z-scheme system contributing to H$_2$ production. An increased amount of α-Fe$_2$O$_3$ in the α-Fe$_2$O$_3$/Zn$_{0.4}$Cd$_{0.6}$S heterostructure reduces the electron mobility, hole diffusion length, and lifetime of charge carriers as the α-Fe$_2$O$_3$ nanoparticles show negative effects resulting in an overall low H$_2$ evolution rate. So an optimum amount of α-Fe$_2$O$_3$ in α-Fe$_2$O$_3$/Zn$_{0.4}$Cd$_{0.6}$S heterostructure is needed to gain better results. The annealing temperature may affect the crystallinity, the surface area, and the

interface contact between α-Fe$_2$O$_3$ and Zn$_{0.4}$Cd$_{0.6}$S, so the effect of calcination temperature on the visible light photocatalytic H$_2$ production was investigated. The visible light photocatalytic hydrogen (H2) production over 10 wt.% α-Fe$_2$O$_3$/Zn$_{0.4}$Cd$_{0.6}$S heterostructure prepared at different temperatures (573, 673, and 773 K) was measured (Fig. 7b). Photocatalytic H$_2$ production over 10 wt.% α-Fe$_2$O$_3$/Zn$_{0.4}$Cd$_{0.6}$S without heat treatment is found to be 70 µmol h^{-1}, while after calcination at different temperatures, the rate of H$_2$ evolution drastically increases, which may be ascribed to strong solid–solid interface formation for efficient charge separation together with decreasing photogenerated e/h recombination through improved crystallinity [34,35]. The photocatalytic H$_2$ production over 10 wt.% α-Fe$_2$O$_3$/Zn$_{0.4}$Cd$_{0.6}$S samples annealed at 573 and 673 K was observed at 169.82 and 536.82 µmol h^{-1}, respectively. When the calcination temperature was increased to 773 K, the rate of H$_2$ evolution decreased (320.82 µmol h^{-1}), presumably due to the decrease in surface area and crystallinity of the as-synthesized sample at high temperature, as supported by BET surface area measurements and XRD results (Table S1, Fig. S7). The BET surface area and pore volume of 10 wt.% α-Fe$_2$O$_3$/Zn$_{0.4}$Cd$_{0.6}$S increases with increasing calcination temperature from 573 to 673 K but significantly decrease when calcination temperature
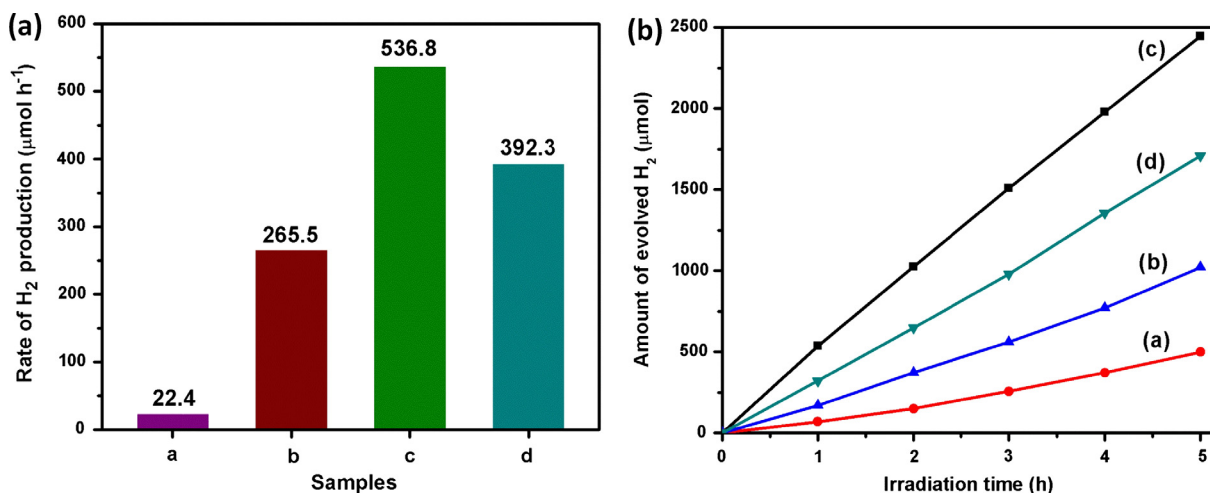

Fig. 7. (a) Photocatalytic hydrogen evolution rates of different samples calcined at 673 K: Zn$_{0.4}$Cd$_{0.6}$S (a), 5 wt.% α-Fe$_2$O$_3$/Zn$_{0.4}$Cd$_{0.6}$S (b), 10 wt.% α-Fe$_2$O$_3$/Zn$_{0.4}$Cd$_{0.6}$S (c), and 15 wt.% α-Fe$_2$O$_3$/Zn$_{0.4}$Cd$_{0.6}$S (d). (b) Time courses of photocatalytic H$_2$ evolution from water solution on 10 wt.% α-Fe$_2$O$_3$/Zn$_{0.4}$Cd$_{0.6}$S prepared at different temperatures: without thermal treatment (a), 573 K (b), 673 K (c), and 773 K (d).

increases to 773 K [36]. The crystallinity also decreases when the calcination temperature increases from 673 to 773 K, which is in agreement with the decrease in activity and BET surface area measurements. FTIR and TGA analysis of 10 wt.% α-Fe$_2$O$_3$/Zn$_{0.4}$Cd$_{0.6}$S heterostructure before and after calcination at 673 K show that PVP is removed from the surface of the catalyst after heat treatment, which favors the enhancement of photocatalytic performance (Figs. S8 and S9). Moreover, HRTEM images of 10 wt.% α-Fe$_2$O$_3$/Zn$_{0.4}$Cd$_{0.6}$S heterostructure calcined at 773 K also show sintering of the catalyst at high temperature, which decreases the activity (Fig. S10).

Most photocatalysts show a decline in activity during the recycling process, which is the main cause for rejection of widespread practical applications. To investigate the stability up to several cycles, the photocatalytic H$_2$ production over 10 wt.% α-Fe$_2$O$_3$/Zn$_{0.4}$Cd$_{0.6}$S was measured four times using the same catalyst under visible light irradiation ($\lambda \geq 420$ nm). As shown in Fig. 8, the 10 wt.% α-Fe$_2$O$_3$/Zn$_{0.4}$Cd$_{0.6}$S heterostructure does not exhibit any obvious decrease in photocatalytic activity up to four consecutive cycles, suggesting the excellent stability of the as-obtained Z-scheme photocatalyst. To verify the stability of the 10 wt.% α-Fe$_2$O$_3$/Zn$_{0.4}$Cd$_{0.6}$S heterostructure after four consecutive cycles, the photocorrosion property was analyzed by inductively coupled plasma mass spectrometry (ICP). The catalyst showed good stability even after four consecutive photocatalytic cycles, which clearly suggests that synthesis and subsequent calcination stabilize the photocatalyst against photocorrosion (Table S2).

The different loading amounts of α-Fe$_2$O$_3$ in the α-Fe$_2$O$_3$/Zn$_{0.4}$Cd$_{0.6}$S heterostructure showed that Zn$_{0.4}$Cd$_{0.6}$S is the leading active component for photocatalytic H$_2$ evolution. The strong interfacial connection between α-Fe$_2$O$_3$ and Zn$_{0.4}$Cd$_{0.6}$S serves as an efficient photogenerated electron transport pathway from the conduction band of α-Fe$_2$O$_3$ to the valence band of Zn$_{0.4}$Cd$_{0.6}$S to capture the photogenerated holes, as represented in Fig. 9. The photogenerated electrons from Zn$_{0.4}$Cd$_{0.6}$S were further captured by H$^+$ and accomplished the reduction process. Fast electron transfer from α-Fe$_2$O$_3$ to Zn$_{0.4}$Cd$_{0.6}$S through the interface leads to efficient charge separation in Zn$_{0.4}$Cd$_{0.6}$S, thus reducing electron-hole pair recombination, resulting in enhanced photocatalytic activity. The photogenerated holes in α-Fe$_2$O$_3$ can be trapped by sacrificial reagents that undergo the oxidation of SO$_3^{2-}$ to SO$_4^{2-}$ [37,38]. This possible Z-scheme mechanism is also supported by the transient photocurrent response and electronic impedance spectroscopy

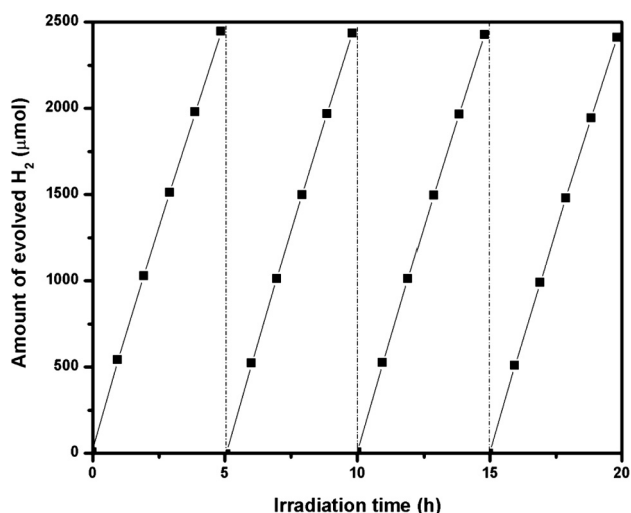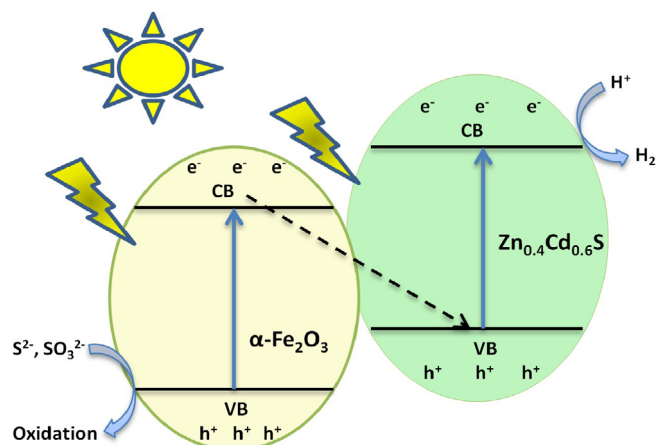**Fig. 9.** A schematic diagram illustrating the charge transfer process for the 10 wt.% α-Fe$_2$O$_3$/Zn$_{0.4}$Cd$_{0.6}$S heterostructure.

results, which suggest a high photocurrent response and much smaller semicircle for the α-Fe$_2$O$_3$/Zn$_{0.4}$Cd$_{0.6}$S heterostructure, leading to an efficient H$_2$ evolution rate. Our multicomponent Z-scheme photocatalyst may hold great potential for solving future energy problems by water splitting and provides an advance toward the development of environmentally friendly, low-cost photocatalysts.

4. Conclusions

In this work, we have developed an α-Fe$_2$O$_3$/Zn$_{0.4}$Cd$_{0.6}$S heterostructure for visible-light-driven hydrogen (H$_2$) production by water splitting. Inspired by the natural photosynthesis process in plants, we followed a multicomponent approach to couple two photocatalysts, forming an interface between them for Z-scheme electron transfer. The photocatalytic activities were observed using solid solutions of the α-Fe$_2$O$_3$/Zn$_{0.4}$Cd$_{0.6}$S heterostructure with Na$_2$S and Na$_2$SO$_3$ as the sacrificial reagent. Our 10 wt.% α-Fe$_2$O$_3$/Zn$_{0.4}$Cd$_{0.6}$S heterostructure exhibits as high as 536.8 μmol h^{-1} photocatalytic H$_2$ production with AQY of 11.2% under visible light ($\lambda > 420$ nm). The enhanced catalytic activity may be attributed to good crystallinity and optimum charge separation efficiencies as indicated by BET, EIS, and photocurrent response results. The UV–vis diffuse reflectance spectra also show that our 10 wt.% α-Fe$_2$O$_3$/Zn$_{0.4}$Cd$_{0.6}$S heterostructure absorbs most of the light from the visible region, which contributes to the enhancement of activity. Our results provide significant progress toward the design of further Z-scheme photocatalysts for practical applications.

Appendix A. Supplementary material

Supplementary data associated with this article can be found, in the online version, at http://dx.doi.org/10.1016/j.jcat.2017.06.019.

Fig. 8. Time-cycle photocatalytic hydrogen production over α-Fe$_2$O$_3$/Zn$_{0.4}$Cd$_{0.6}$S heterostructure under visible-light illumination ($\lambda \geq 420$ nm).

References

[1] X.B. Chen, S.H. Shen, L.J. Guo, S.S. Mao, Semiconductor-based photocatalytic hydrogen generation, Chem. Rev. 110 (2010) 6503–6570.

[2] J.A. Turner, Sustainable hydrogen production, Science 305 (2004) 972–974.

[3] M. Matsuoka, M. Kitano, M. Takeuchi, K. Tsujimaru, M. Anpo, J.M. Thomas, Photocatalysis for new energy production: recent advances in photocatalytic water splitting reactions for hydrogen production, Catal. Today 122 (2007) 51–61.

[4] Z.G. Zou, J.H. Ye, K. Sayama, H. Arakawa, Direct splitting of water under visible light irradiation with an oxide semiconductor photocatalyst, Nature 414 (2001) 625–627.

[5] H. Kato, K. Asakura, A. Kudo, Highly efficient water splitting into H_2 and O_2 over lanthanum-doped $NaTaO_3$ photocatalysts with high crystallinity and surface nanostructure, J. Am. Chem. Soc. 125 (2003) 3082–3089.

[6] J.S. Jang, H.G. Kim, J.S. Lee, Heterojunction semiconductors: a strategy to develop efficient photocatalytic materials for visible light water splitting, Catal. Today 185 (2012) 270–277.

[7] A.J. Bard, Photoelectrochemistry and heterogeneous photo-catalysis at semiconductors, J. Photochem. 10 (1979) 59–75.

[8] P. Zhou, J. Yu, M. Jaroniec, All-solid-state Z-scheme photocatalytic systems, Adv. Mater. 26 (2014) 4920–4935.

[9] H. Tada, T. Mitsui, T. Kiyonaga, T. Akita, K. Tanaka, All-solid-state Z-scheme in CdS–Au–TiO$_2$ three-component nanojunction system, Nat. Mater. 5 (2006) 782–786.

[10] T. Arai, S. Sato, T. Kajino, T. Morikawa, Solar CO_2 reduction using H_2O by a semiconductor/metal-complex hybrid photocatalyst: enhanced efficiency and demonstration of a wireless system using $SrTiO_3$ photoanodes, Energy Environ. Sci. 6 (2013) 1274–1282.

[11] J.F. Reber, M. Rusek, Photochemical hydrogen production with platinized suspensions of cadmium sulfide and cadmium zinc sulfide modified by silver sulfide, J. Phys. Chem. 90 (1986) 824–834.

[12] C. Xing, Y. Zhang, W. Yan, L. Guo, Band structure-controlled solid solution of $Cd_{1-x}Zn_xS$ image image photocatalyst for hydrogen production by water splitting, Int. J. Hydrogen Energy 31 (2006) 2018–2024.

[13] L. Shang, B. Tong, H.J. Yu, I.G.I.N. Waterhouse, C. Zhou, Y.F. Zhao, M. Tahir, L.Z. Wu, C.H. Tung, T.R. Zhang, Hydrogen evolution: CdS nanoparticle-decorated Cd nanosheets for efficient visible light-driven photocatalytic hydrogen evolution, Adv. Energy Mater. 6 (2016) 1501241.

[14] A.P. Wu, L.Q. Jing, J.Q. Wang, Y. Qu, Y. Xie, B.J. Jiang, C.G. Tian, H.G. Fu, ZnO-dotted porous ZnS cluster microspheres for high efficient, Pt-free photocatalytic hydrogen evolution, Sci. Rep. 5 (2015) 8858.

[15] Y.B. Wang, J.C. Wu, J.W. Zheng, R. Xu, Highly active $Zn_xCd_{1-x}S$ photocatalysts containing earth abundant elements only for H_2 production from water under visible light, Catal. Sci. Technol. 1 (2011) 940–947.

[16] B.Q. Lu, N. Ma, Y.P. Wang, Y.W. Qiu, H.H. Hub, J.H. Zhao, D.Y. Liang, S. Xu, X.Y. Li, Z.Y. Zhu, C. Cui, Visible-light-driven $TiO_2/Ag_3PO_4/GO$ heterostructure photocatalyst with dual-channel for photo-generated charges separation, J. Alloys Comp. 630 (2015) 163–171.

[17] X.L. Yin, L.L. Li, W.J. Jiang, Y. Zhang, X. Zhang, L.J. Wan, J.S. Hu, MoS_2/CdS nanosheets-on-nanorod heterostructure for highly efficient photocatalytic H_2 generation under visible light irradiation, ACS Appl. Mater. Interfaces 8 (2016) 15258–15266.

[18] J.C. Wang, L. Zhang, W.X. Fang, J. Ren, Y.Y. Li, H.C. Yao, J.S. Wang, Z.J. Li, Enhanced photoreduction CO_2 activity over direct Z-scheme α-Fe_2O_3/Cu_2O heterostructures under visible light irradiation, ACS Appl. Mater. Interfaces 7 (2015) 8631–8639.

[19] A.L. Linsebigler, G.Q. Lu, J.T. Yates, Photocatalysis on TiO_2 surfaces: principles, mechanisms, and selected results, Chem. Rev. 95 (1995) 735–758.

[20] W. Liu, J.S. Dennis, S.A. Scott, The effect of addition of ZrO_2 to Fe_2O_3 for hydrogen production by chemical looping, Ind. Eng. Chem. Res. 51 (2012) 16597–16609.

[21] X.D. Li, Z. Wang, Z.M. Zhang, L.L. Chen, J.L. Cheng, W. Ni, B. Wang, E.Q. Xie, Light illuminated α-Fe_2O_3/Pt nanoparticles as water activation agent for photoelectrochemical water splitting, Sci. Rep. 5 (2015) 9130.

[22] A. Boudjemaa, M. Trari, Photo-catalytic hydrogen production over Fe_2O_3 based catalysts, Int. J. Hydrogen Energy 35 (2010) 7684–7689.

[23] P. Mirtchev, K. Liao, E. Jaluague, Q. Qiao, Y. Tian, M. Varela, K.S. Burch, S.J. Pennycook, D.D. Perovic, G. Ozin, Fe_2O_3/Cu_2O heterostructured nanocrystals, J. Mater. Chem. A 2 (2014) 8525–8533.

[24] H. Jiang, H.F. Ma, Y. Jin, L.F. Wang, F. Gao, Q.Y. Lu, Hybrid α-Fe_2O_3@$Ni(OH)_2$ nanosheet composite for high-rate-performance supercapacitor electrode, Sci. Rep. 6 (2016) 31751.

[25] M.S. Akhtar, M.A. Malik, S. Riaz, S. Naseem, Room temperature ferromagnetism and half metallicity in nickel doped ZnS: experimental and DFT studies, Mater. Chem. Phys. 160 (2015) 440–446.

[26] N. Biswal, D.P. Das, S. Martha, K.M. Parida, Efficient hydrogen production by composite photocatalyst CdS–ZnS/Zirconium–titanium phosphate (ZTP) under visible light illumination, Int. J. Hydrogen Energy 36 (2011) 13452–13460.

[27] X. Xu, R.J. Lu, X.F. Zhao, Y. Zhu, S.L. Xu, F.Z. Zhang, Novel mesoporous $ZnxCd_{1-x}S$ nanoparticles as highly efficient photocatalysts, Appl. Catal. B 125 (2012) 11–20.

[28] P.P. Wang, X.X. Zou, L.L. Feng, J. Zhao, P.P. Jin, R.F. Xuan, Y. Tian, G.D. Lia, Y.C. Zou, Facile synthesis of single-crystalline hollow α-Fe_2O_3 nanospheres with gas sensing properties, RSC Adv. 4 (2014) 38707–38710.

[29] X. Zhou, J. Jin, X.J. Zhu, J. Huang, J.G. Yu, W.Y. Wong, W.X. Wong, New $Co(OH)_2$/CdS nanowires for efficient visible light photocatalytic hydrogen production, J. Mater. Chem. A 4 (2016) 5282–5287.

[30] R.Q. Ye, H.B. Fang, Y.Z. Zheng, N. Li, Y. Wang, X. Tao, Fabrication of $CoTiO_3$/g-C_3N_4 hybrid photocatalysts with enhanced H_2 evolution: Z-scheme photocatalytic mechanism insight, ACS Appl. Mater. Interfaces 8 (2016) 13879–13889.

[31] Q. Wang, T. Hisatomi, Q.X. Jia, H. Tokudome, M. Zhong, C.Z. Wang, Z.H. Pan, T. Takata, M. Nakabayashi, N. Shibata, Y.B. Li, I.D. Sharp, A. Kudo, T. Yamada, K. Domen, Scalable water splitting on particulate photocatalyst sheets with a solar-to-hydrogen energy conversion efficiency exceeding 1%, Nat. Mater. 15 (2016) 611–615.

[32] T.H. Yang, L.D. Huang, Y.W. Harn, C.C. Lin, J.K. Chang, C.I. Wu, J.M. Wu, High density unaggregated Au nanoparticles on ZnO nanorod arrays function as efficient and recyclable photocatalysts for environmental purification, Small 9 (2013) 3169–3182.

[33] K. Maeda, Z-scheme water splitting using two different semiconductor photocatalysts, ACS Catal. 3 (2013) 1486–1503.

[34] X. Zong, G.P. Wu, H.J. Yan, G.J. Ma, J.Y. Shi, F.Y. Wen, L. Wang, C. Li, Photocatalytic H_2 evolution on MoS_2/CdS catalysts under visible light irradiation, J. Phys. Chem. C 114 (2010) 1963–1968.

[35] X. Wang, G. Liu, L. Wang, Z. Chen, G.Q. Lu, H.M. Cheng, ZnO–CdS@Cd Heterostructure for effective photocatalytic hydrogen generation, Adv. Energy Mater. 2 (2012) 42.

[36] S.N. Tijare, M.V. Joshi, P.S. Padole, P.A. Mangrulkar, S.S. Rayalu, N.K. Labhsetwar, Photocatalytic hydrogen generation through water splitting on nano-crystalline $LaFeO_3$ perovskite, Int. J. Hydrogen Energy 37 (2012) 10451–10456.

[37] J.G. Yu, S.H. Wang, J.X. Low, W. Xiao, Enhanced photocatalytic performance of direct Z-scheme g-C_3N_4–TiO_2 photocatalysts for the decomposition of formaldehyde in air, Phys. Chem. Chem. Phys. 15 (2013) 16883–16890.

[38] X.W. Wang, G. Liu, L.Z. Wang, J. Pan, G.Q. Lu, H.M. Cheng, TiO_2 films with oriented anatase 001 facets and their photoelectrochemical behavior as CdS nanoparticle sensitized photoanodes, J. Mater. Chem. 21 (2011) 869–873.